Fizika Nizkikh Temperatur, 2006, v. 32, No. 2, p. 176–183

Magnetic and transport properties of charge ordered $La_{0.5}Ca_{0.5}MnO_3$ and $La_{0.4}Ca_{0.6}MnO_3$ films

V.G. Prokhorov, V.A. Komashko, and G.G. Kaminsky

Institute of Metal Physics, National Academy of Sciences of Ukraine
36 Vernadskogo Ave., Kiev, 03142, Ukraine
E-mail: pvg@imp.kiev.ua

Y.P. Lee, S.Y. Park, and Y.H. Hyun

Quantum Photonic Science Research Center and Department of Physics
Hanyang University, Seoul 133-791, Korea

V.L. Svetchnikov

National Center for HREM, TU Delft 2628AL, The Netherlands

K.W. Kim

Department of Physics, Sunmoon University, Asan, Choongnam 336-840, Korea

J.Y. Rhee

BK21 Physics Research Division and Institute of Basic Science, Sungkyunkwan University
Suwon 440-746, Korea

Received July 15, 2005

The magnetic and the transport properties of $La_{0.5}Ca_{0.5}MnO_3$ and $La_{0.4}Ca_{0.6}MnO_3$ films with different thickness, prepared by rf-magnetron sputtering by using the so-called «soft» (or powder) target on $LaAlO_3$ substrate, have been investigated. The electron-diffraction and the high-resolution electron microscopy (HREM) studies show that the charge-ordered phase is observed at room temperature for all films. Both the paramagnetic-to-ferromagnetic transition at $T_C \approx 250$ K upon cooling and the appearance of an antiferromagnetic (AFM) phase at $T_N \lesssim 140$ K were observed in the $La_{0.5}Ca_{0.5}MnO_3$ films, while the $La_{0.4}Ca_{0.6}MnO_3$ films exhibited the AFM transition only at the same temperature, excepting the small ferromagnetic (FM) response from a «dead» layer. It was shown that the volume fraction of the FM phase in the $La_{0.5}Ca_{0.5}MnO_3$ film did not exceed of and the FM phase coexisted with the AFM one at low temperature. All films manifest an exponential temperature dependence of resistance without evidence of the metal-insulator transition. This is explained by the scarcity of the FM phase for the formation of infinite percolating cluster and by an existence of the charge-ordered phase. The field-dependent magnetoresistance at low temperature is described in terms of the spin-assisted polaron-hopping model.

PACS: **75.70.-i**, **75.47.-m**, **71.30.+h**

Keywords: colossal magnetoresistance, manganite films, charge ordering, polaronic transport

1. Introduction

The hole-doped perovskite manganites $L_{1-x}A_xMnO_3$, where L and A are a trivalent lanthanide and a divalent alkaline-earth ions, respectively, have attracted considerable attention due to their interesting fundamental science and potential for applications [1]. It has been shown that the spin, charge, and lattice are strongly coupled with each other in these compounds and may be considered as strongly correlated systems [2]. A complex interplay of charge, lattice, spin, and

orbital degrees of freedom in these systems leads to the complicated phase diagram of $L_{1-x}A_xMnO_3$ and is not completely understood. As the composition x changes, they show a variety of phenomena, such as ferromagnetic (FM), antiferromagnetic (AFM), charge (CO) and orbital (OO) ordering. $La_{1-x}Ca_xMnO_3$ is a typical system which demonstrates the change of the ground state from FM metal to CO AFM insulator, when the Ca doping level crosses 0.5 [3]. It was shown that, upon lowering the temperature, the $La_{0.5}Ca_{0.5}MnO_3$ compound first underwent a paramagnetic (PM)-to-FM phase transition at $T_C \simeq 225$ K and then become the CO AFM phase at $T_{CO} \simeq T_N \simeq 225$ K [4]. In the letter case the transition is attributed to the well-known charge-exchange-type AFM ordering, which has been proposed long ago by Goodenough [5], and observed by Wollan and Koehler in this compound [6]. The low-temperature phase with rich Mn^{4+} hole doping ($x > 0.5$) is AFM and insulating [7–10]. Nevertheless, numerous contradictory experimental data on the magnetic and transport properties for this composition can be found in the literature. There are, for example, the observation of a ferromagnetic residual magnetization [3,11–13] and a metallic-like behavior of the resistivity [14–16] of $La_{0.5}Ca_{0.5}MnO_3$ below T_{CO}. These discrepancies were explained by the phase-separation effect and by the coexistence of the different magnetic and electronic phases in the wide temperature range, which were recently observed experimentally [4,17–21]. However, the origin of these inhomogeneities in the magnetic and the electronic states is not clear. There are some trends to explan this feature in the framework of the electronic-phase-separation scenario proposed for manganites [22], but it is more probable that such a behavior can be mainly attributed to the structural inhomogeneities of the samples.

The situation is significantly complicated by the fact that the magnetic and the transport properties of manganites are strongly dependent upon the cation size, the lattice strain, and the microstructure. It is believed that the cooperative Jahn–Teller effect plays an important role in the formation of the ground state of colossal-magnetoresistance materials [23,24] and the insulating CO state can be controlled by a long-range strain [25]. Recently evidence was presented for the appearance of the CO insulating phase in $La_{1-x}Ca_xMnO_3$ films at low temperatures with $x \approx 0.3$ [26–28], while the films with 0.52 demonstrated only the FM metallic ground state through the whole temperature range [29]. In both cases the disagreement with the experimental data for bulk materials was explained by the lattice strains, which are accumulated during the deposition of thin film. Consequently, the magnetic and electronic phase diagrams for $La_{1-x}Ca_xMnO_3$ thin films can be significantly different from that for the bulk and, therefore, it is desirable to peform an additional experimental study. In this paper we report some peculiar results for $La_{0.5}Ca_{0.5}MnO_3$ and $La_{0.4}Ca_{0.6}MnO_3$ films.

2. Experimental techniques

All films were prepared by rf-magnetron sputtering by using the so-called «soft» (or powder) target [30]. The total pressure in chamber was $5 \cdot 10^{-2}$ Torr with a gas mixture of Ar and O_2 (3 : 1). The substrate was a pseudocubic $LaAlO_3$ (001) single crystal with a lattice parameter $\simeq 0.379$ nm. The substrate temperature during the deposition was 750 °C. Under these conditions were deposited the $La_{0.5}Ca_{0.5}MnO_3$ (LCM05) and the $La_{0.4}Ca_{0.6}MnO_3$ (LCM06) films with different thicknesses: $\simeq 30$ nm and $\simeq 100$ nm. The θ–2θ x-ray diffraction (XRD) patterns were obtained by using a Rigaku diffractometer with Cu K_α radiation. The lattice parameters evaluated directly from the XRD data were plotted against $\cos^2\theta/\sin\theta$. From the intercept of the extrapolated straight line to $\cos^2\theta/\sin\theta = 0$, a more precise lattice parameter was obtained. The high-resolution electronmicroscopy (HREM) studies were carried out by using a Philips CM300UT-FEG microscope with a field emission gun operated at 300 kV. The resolution of the microscope was of the order of 0.12 nm. The cross-sectional specimens were prepared by the standard techniques using mechanical polishing followed by ion-beam milling at a grazing incidence. All microstructure measurements were carried out at room temperature. The resistance measurements were performed by using the four-probe method in a temperature range of 4.2–300 K and in a magnetic field up to 5 T. The geometrical dimensions of samples were specified by photolithographic technique: width was 1.0 mm, distance between potential contacts was 6 mm, and length was 10 nm. The value of a dc transport current was 10 μA. The current-source-mode was used for the recording of resistance. The applied magnetic field was directed parallel to the film surface and perpendicular to the current flow. The in-plane field-cooled (FC) and the zero-field-cooled (ZFC) magnetization curves under an applied magnetic field of 100 Oe and the magnetization hysteresis loops were taken with a Quantum Design SQUID magnetometer [31].

3. Microstructure and evidence of charge ordering

Figure 1 presents the (002) and the (004) Bragg peaks for the investigated films. The LCM05 films dis-

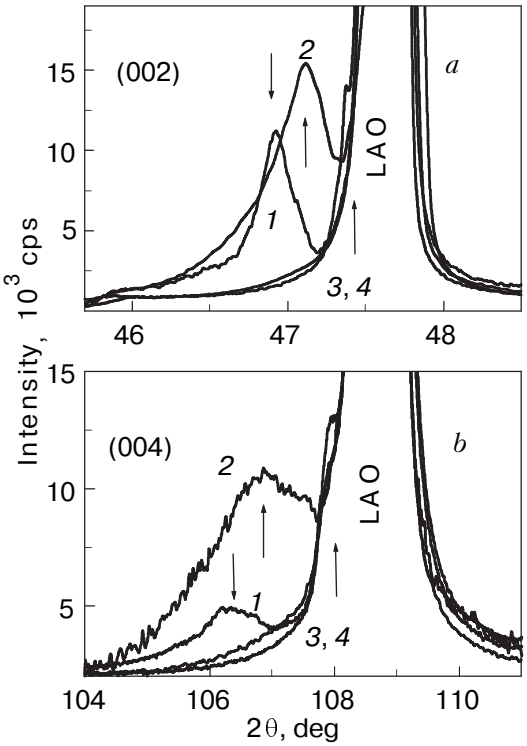

Fig. 1. (002) (*a*) and (004) (*b*) Bragg peaks: 30- (*1*) and 100-nm (*2*) thicknesses for LCM05; and 30- (*3*) and 100-nm (*4*) for LCM06. LAO indicates the Bragg peacks for the substrate.

play the well-defined peaks for $d \simeq 30$ nm (*1*) and 100 nm (*2*), which correspond to the out-of-plane lattice parameter c of 0.3812 nm and 0.3810 nm, respectively, for the cubic symmetry. The obtained results agree well with the published data for both film and bulk compound [10,20,32]. The Bragg peaks of the LCM06 films are located very close to those of the substrate (peaks *3* and *4*), corresponding to $c \simeq 0.38$ nm for both film thicknesses, and are coincident with that for bulk [10,32].

The cross-sectional low-magnification HREM image and electron diffraction (ED) pattern of the LCM05 film ($d \simeq 100$ nm) are displayed in Fig. 2,*a*. The HREM image exhibits sharp, flat and well defined interface between the substrate and the film (indicated by the black arrow) while the very thin (≥ 1 nm) intermediate (or «dead») layer on the film side is also present. The ED pattern can be indexed as the well-known orthorhombic crystal structure with a small orthorhombic distortion: $a \approx b \approx \sqrt{2}a_p$ and $c \approx 2a_p$, where a_p is the lattice parameter of the simple perovskite structure. Figures 2,*b* and 2,*c* show the high-magnification HREM images of the film and the «dead» layer, respectively. Insets are the corresponding fast-Fourier-transform (FFT) patterns. It is seen that, in the first case, FFT produces a rectangular pattern of the spots, which is typical for a regular crystal

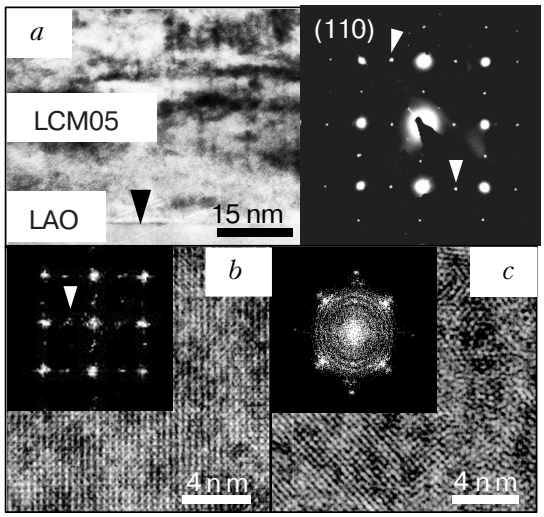

Fig. 2. Low-magnification cross-sectional HREM image for LCM05 (100 nm). Inset displays the electron diffraction pattern (*a*). High-magnification HREM images of the middle (*b*) and the bottom (close to the «dead» layer) areas of the film (*c*). Insets are FFT patterns of the corresponding images.

lattice, while in the second one the FFT pattern displays smeared spots and slightly ring-like traces, typical for a randomly oriented mosaic microstructure. Analysis of ED and HREM data for the LCM05 film reveals that the estimated lattice parameter $a_p \simeq 0.382$ nm is almost identical to that obtained by the XRD data. At the same time, well-defined superlattice spots are evident for the (1/2, 0, 0) or (0, 1/2, 0) positions in additional to the fundamental Bragg reflections, which are indicated by the white arrows in the insets of Figs. 2,*a* and 2,*b*. Similar superlattice spots in ED pattern were observed in $La_{0.5}Ca_{0.5}MnO_3$ at $T = 95$ K and treated as the appearance of a charge ordering of Mn^{4+} and Mn^{3+} ions [33]. Therefore, one can conclude that the CO state occurs in the LCM05 film above the room temperature.

Figure 3 displays results of the same HREM study carried out for the LCM06 film with $d = 100$ nm. The «dead» layer of this film is much larger than that in LCM05 and reaches 10 nm. The ED pattern, displayed in the inset, also exhibits the superlattice spots similar to the LCM05 films, which evidently indicates the existence of the CO state at room temperature. An analysis of the high-magnification HREM images reveals that the LCM06 films have an orthorhombic crystal structure with $a_p \simeq 0.38$ nm. Figures 3,*a* and 3,*b* display the microstructures of the film and the «dead» layer, respectively. Similar to the case of LCM05, FFT produces a rectangular pattern of well defined spots in the former (with slight traces of additional sub erlattice spots), caused by the formation of a perfect crystalline structure, while they are smeared in

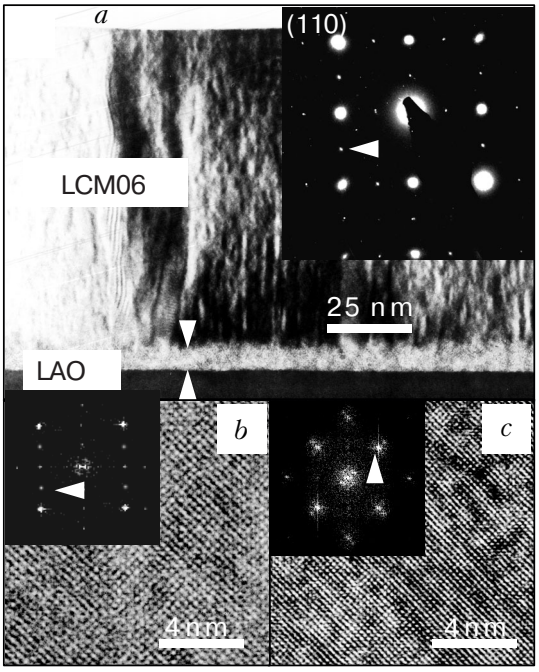

Fig. 3. Low-magnification cross-sectional HREM image for LCM06 (100 nm). Inset displays the electron diffraction pattern (*a*). High-magnification HREM images of the film (*b*) and the «dead» layer (*c*). Insets are FFT patterns of the corresponding images.

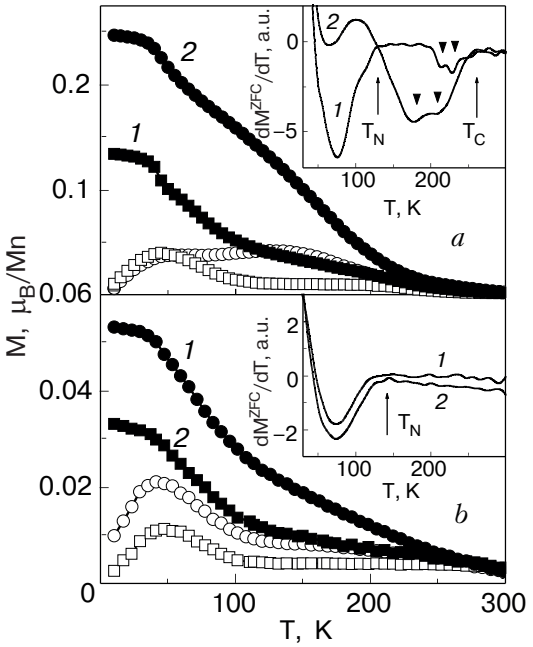

Fig. 4. Field-cooled (solid) and zero-field-cooled (open) magnetization curves for the LCM05 (*a*) and the LCM06 (*b*) films of 30- (*1*) and 100-nm (*2*) thicknesses under an in-plane magnetic field of 100 Oe. Insets display the first derivatives of corresponding ZFC $M(T)$ dependencies. Arrows indicate the onset of FM and AFM transition. Triangles indicate the two-stage FM transition in the LCM05 films.

the bright halos and slightly split in the latter. Therefore, we can conclude that the «dead» layer has a nanocrystalline mosaic structure.

4. Experimental results

4.1 Magnetic properties

Figures 4,*a* and 4,*b* present the in-plane FC and ZFC temperature dependencies of the magnetization, $M(T)$, for the LCM05 (*a*) and LCM06 (*b*) film with $d \simeq 30$ nm (*1*) and 100 nm (*2*), respectively, measured under an applied magnetic field of 100 Oe. Both samples of LCM05 demonstrate the PM–to–FM magnetic transition at $T_C \approx 250$ K and an appearance of the AFM phase at $T_N \lesssim 140$ K. These temperatures were obtained from the analysis of the first derivative of ZFC $M(T)$–versus–T curves, which are displayed in the inset in Fig. 4,*a*. Both the FM and the AFM transitions are well defined for the thinner film, while the onset of the AFM ordering is barely discernible for the thick one, owing to the presence of larger volume of the FM phase. Moreover, the inset also displays a two-peaks behavior of dM^{ZFC}/dT–versus–T in the range of the FM transition, indicating the presence of two Curie points, which are slightly separated from each other. The two-peak behavior can be explained by the existence of inhomogeneous microstructures in this film near the substrate, revealed by the HREM study. One can suggest that with decreasing temperature the FM phase appears first inside of the film and then into the «dead» layer.

An analysis of the dM^{ZFC}/dT–versus–T curves for LCM06, displayed in the inset in Fig. 4,*b*, reveals that both films with different thicknesses manifest the AFM transition at $T_N \approx 140$ K only. At the same time, the large difference between ZFC and FC $M(T)$ curves above T_N suggests the presence of a small volume of the FM phase.

Figures 5,*a* and 5,*b* show the in-plane magnetic hysteresis loops, $M(T)$, at 10 K for the LCM05 (*a*) and the LCM06 (*b*) films with (*1*) $d \simeq 30$ nm and (*2*) 100 nm, respectively. Although the LCM05 films show the FM transition at $T_C \approx 250$ K [see Fig. 4,*a*], it is not clear whether the volume of the FM phase remains the same below T_N. For comparison, the $M(T)$ dependence for the $La_{0.7}Ca_{0.3}MnO_3$ film [curve *3* in Fig. 5,*a*], deposited on the $LaAlO_3$ substrate with the thickness of 100 nm is shown. It is seen that the saturated magnetic moment of the $La_{0.7}Ca_{0.3}MnO_3$ film is $\simeq 3.2\ \mu_B/Mn$, which is close to the theoretical value of an average effective magnetic moment for a fully FM sample ($\mu_{eff} \simeq 3.5\ \mu_B/Mn$). On the other hand, the saturated magnetic moment for both the LCM05

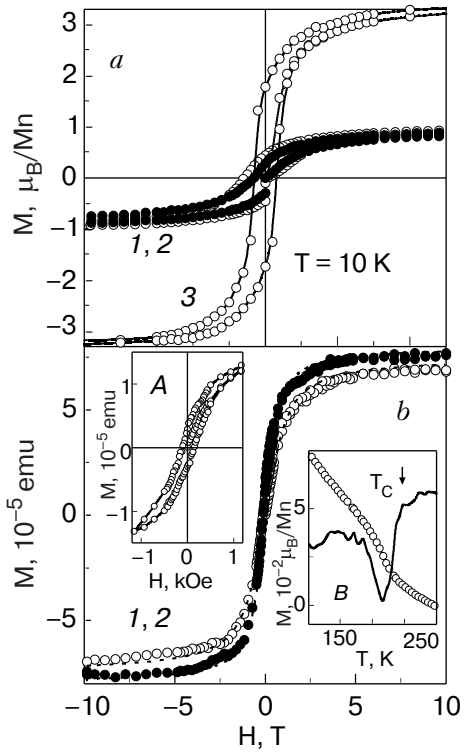

Fig. 5. In-plane hysteresis loops of LCM05 (*a*) and LCM06 (*b*) at 10 K, respectively, for 30 (solid symbols) and 100 nm (open symbols) thickness. Curve (*3*) in (*a*) corresponds to the $La_{0.7}Ca_{0.3}MnO_3$ film. Inset *A* in (*b*) exhibits the low-field hysteresis loop of the 100-nm-thickness LCM06 film in detail. Inset *B* in (*b*) displays the $M(T)$ dependence at magnetic field of 2 kOe (open symbols) and the corresponding first derivative (solid line) for the same film. Lines are guides to the eyes.

films is 0.95 μ_B/Mn. Taking into account the fact that whole volume of the $La_{0.7}Ca_{0.3}MnO_3$ film becomes ferromagnetic at low temperature, one can conclude that $\simeq$ 30% of the volume of the LCM05 film belongs to the FM phase, that is almost coincident with the published results for the bulk [21]. Therefore, the LCM05 films exhibit the coexistence of the FM and the AFM phases at low temperature and can be treated as a magnetically inhomogeneous systems. Figure 5,*b* shows that the LCM06 films demonstrate almost anhysteretic magnetization loops, as it is represented by the inset (*A*), with the coercive field $H_c \simeq 100$ Oe, while the LCM05 films have $H_c \simeq 600$ Oe. This fact suggests that we deal with a superparamagnetic (SPM) rather than a real FM state in these films. It is reasonable to assume that such type of magnetic state can occur in the «dead» layer, which has nanocrystalline disordered microstructures. On the other hand, the $M(T)$ dependence measured under applied magnetic field of 2 kOe manifests the FM response around 250 K [see inset (*B*) in Fig. 5,*b*].

4.2. Transport properties

Figure 6 shows the temperature dependences of resistance, $R(T)$, for the LCM05 (*1*, *2*) and the LCM06 (*3*, *4*) films with (open symbols) and without (solid symbols) an applied magnetic field of 5 T. The experimental curves reveal an exponential $R(T)$ behavior in the whole temperature range, which is cleary shown as the linear behavior in the ln (R/T)–versus–T^{-1} plots (see the inset of Fig. 6), and is almost insensitive to the applied magnetic field. This is typical characteristics of the bulk sample with the same composition. Therefore, we did not find the evidence of the MI transition in the films.

Figure 7 displays the magnetic-field dependence of the negative magnetoresistance (MR) for the LCM05 (*a*) and the LCM06 (*b*) films at T = 10 K. The MR value is defined by 100% × $[R(H) - R(0)]/R(H)$ where $R(H)$ and $R(0)$ are the resistances with and without the magnetic field, respectively. It is seen that MR does not exceed of 5% in the applied magnetic field of 2 T.

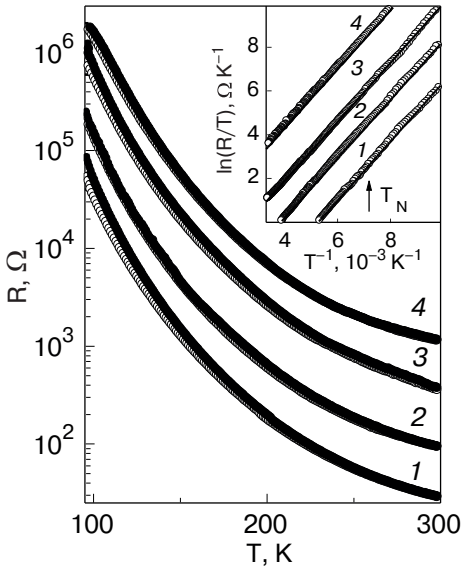

Fig. 6. Temperature dependence of the resistance for LCM05 of 100- (*1*) and 30- (*2*) and for LCM06 of 100- (*3*) and 30-nm (*4*) thicknesses without (solid symbols) and with (open symbols) an applied magnetic field of 5 T. Inset displays the corresponding ln(R/T)–versus–T^{-1} plots. Solid lines are fitting curves for the thermally activated conductivity approximation. Arrow indicates temperature of the AFM transition.

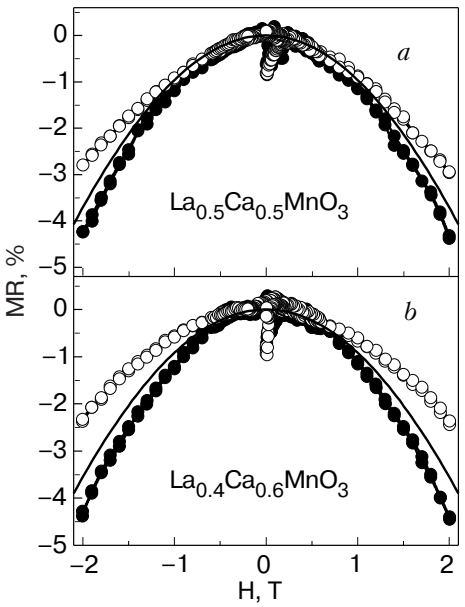

Fig. 7. Magnetic-field dependence of MR ratio for LCM05 (*a*) and LCM06 (*b*) of 100 (solid symbols) and 30 nm (open symbols) thickness at 10 K. Solid lines are theoretical curves obtained in the framework of a spin-assisted polaron hopping approach.

5. Discussion

5.1. Influence of «dead» layer on magnetic properties

Let us consider the magnetic properties of the investigated samples. The LCM05 films manifest the $M(T)$ dependence, which agrees well with a magnetic phase diagram for this composition [3,4,8,9,32]. Both FM and the AFM magnetic transitions are observed with decreasing temperature at $T_C \approx 250$ K and $T_N \lesssim 140$ K, respectively. The observed two-stage behavior of the FM ordering is explained by the presence of the thin «dead» layer with disordered microstructure. In contrast, the LCM06 films exhibit not only the AFM transition at $T_N \approx 140$ K, which is typical for this composition, but also an additional magnetic transition at a higher temperature. Inset *B* in Fig. 5,*b* shows the remarkable increase in $M(T)$ at ≈ 250 K under an applied magnetic field of 2 kOe, while the similar peculiarity is not observed on the ZFC $M(T)$ curves at low applied magnetic field of 100 Oe. This indicates that, though the long-range spontaneous magnetization does not appear in the film, the small-size randomly-oriented FM clusters are present at $T \lesssim 250$ K. On the other hand, Fig. 5,*a* displays that the directly measured value of the saturated magnetic moment, M_s, is the same for both films, in spite of the almost three times difference in their thickness: 30 and 100 nm for curves *1* and *2*, respectively. Consequently, the volume of the FM phase does not depend on the film thickness and can be associated with the presence of the nanocrystalline 10-nm-thickness «dead» layer in both films. This is further confirmed by the comparison with the M_s value for the fully ferromagnetic $La_{0.7}Ca_{0.3}MnO_3$ ($\simeq 9.2 \cdot 10^{-4}$ emu) and the LCM06 film ($\simeq 7.5 \cdot 10^{-5}$ emu) with the equal thickness and area. The estimated volume fraction of the FM phase in LCM06 (8) is almost coincident with the relative volume of «dead» layer (10), verified by the HREM study.

5.2. Spin-assisted polaron transport in AFM CO state

Now let us consider the transport properties of the films. Figure 6 exhibits that all the films, independent of composition and thickness, manifest an exponential $R(T)$ dependence in the whole investigated temperature range. Therefore, we did not find the evidence of the MI transition in our films, while some publications claim its presence at these compositions [14–16,29,34,35]. Because the volume of the FM phase in the LCM05 film ($\simeq 30\%$) is smaller than the threshold value ($\simeq 40\%$) of a percolation for 3-dimensional systems [36], the MI transition can not be expected in this sample [22]. A similar argument can be applied to the LCM06 films, in which the FM ordered phase is located in «dead» layer only and occupies the negligible fraction of the film volume. At the same time, we did not observe any peculiarities on the $R(T)$ curves, which could be treated as the formation of a CO state. The $\ln(R/T)$–versus–T^{-1} plots represented by the inset in Fig. 6 manifest the straight lines for all films in the whole temperature range, even near the AFM transition. The absence of CO transition suggests us that it may occur at higher temperature. This agrees with the ED data which indicate the existence of the CO state in the film already at room temperature. Therefore, one can suggest that the thermally activated polaronic transport is dominating in the films at low temperature because the charge ordering and the antiparallel spin orientation of neighboring ions lead to the blocking of a nonadiabatic through-the-barrier tunneling of carriers. It is supported by an excellent agreement between the experimental $R(T)$ dependencies and the theoretical curves obtained on the basis of thermally activated conductivity model, $R(T) = R_0 T \exp(T_A/T)$, where T_A is the activation energy in unit of temperature (indicated by solid lines in the inset of Fig. 6). The activation energy turn out to be $T_A \simeq 1350$ K for all films. According to Appel [37] the hopping probability of insulator with a short-range magnetic ordering should be modified by a multiplicative term $(1 + M^2/M_s^2)/2$. In this case the negative magnetoresistance ratio, represented by Fig. 7,

can be expressed by $MR(\%) = M^2/M_s^2$ and its magnetic-field dependence should be duplicates the squared reduced value of the magnetic moment. The solid lines in Fig. 7 are the theoretical curves representing the squared Langevin function, $L(a) = \coth(a) - 1/a$, where $a = \mu H/k_B$ and μ is effective magnetic moment of the magnetic ion [38]. The μ value for each composition of the film can be estimated from the expression:

$$\mu = g\sqrt{xS_1(S_1 + 1) + (1 - x)S_2(S_2 + 1)},$$

where x is the Ca concentration, $S_1 = 3/2$ and $S_2 = 2$ are the spin values of Mn^{4+} and Mn^{3+} ions, respectively, and $g = 2$ is the Landé factor. The obtained values $\mu \simeq 4.4$ and 4.3 μ_B for LCM05 and LCM06, respectively, were used in the theoretical curves. It is seen that the theoretical curves, obtained without any fitting parameters, almost coincide with experimental data, especially for thick films. Therefore, although this approximation is more suitable for an analysis of the charge transport in the paramagnetic insulating state, it can also be successfully used for the description of the magnetotransport properties in AFM insulating state.

The appearance of CO state at high temperature in the films is probably triggered by a ferroelastic phase transition in LAO substrate which occurs at $T = 544$ °C [39]. The elastic stresses generated in the film during the orthorhombic-to-rhombohedral structural transformation of the LAO substrate stimulate the transition of the film in more stable state at higher temperature than that is predicted by the equilibrium phase diagram.

6. Conclusions

The $La_{1-x}Ca_xMnO_3$ films with $x = 0.5$ (LCM05) and 0.6 (LCM06) were prepared by rf-magnetron sputtering using the «soft» (or powder) target. The LCM05 film demonstrates the PM-to-FM magnetic transition at $T_C \approx 250$ K and the appearance of an AFM phase at $T_N \lesssim 140$ K, while the LCM06 one manifests the AFM transition only at the same temperature and the presence of a small volume (8%) of FM phase in the «dead» layer. It was shown that volume fraction of the FM phase in LCM05 reaches of 30% at 10 K and the FM phase coexists with the AFM phase at low temperature. All films manifest an exponential $R(T)$ dependence in the whole temperature range without the evidence of the MI transition. It is explained by the scarcity of FM phase for the formation of an infinite percolating cluster and by the appearance of CO state at $T \geq 300$ K, according to the ED data. The field-dependent magnetoresistance at low temperature can be described on the basis of the spin-assisted polaron hopping approach.

This work was supported by the KOSEF through the Quantum Photonic Science Research Center, by Korea Research Foundation Grant (KRF-2001-015-DS0015), and by MOST, Korea.

1. For a Review, see *Colossal Magnetoresistance, Charge Ordering and Related Properties of Manganese Oxides*, C.N.R. Rao and B. Raveau (eds.), Wold Scientific, Singapore (1998) and Colossal Magnetoresistance Oxides, Y. Tokura (ed.), Gordon and Breach, London (1999).
2. N.D. Mathur and P.B. Littlewood, *Phys. Today* **56**, 25 (2003).
3. P. Schiffer, A.P. Ramirez, W. Bao, and S.-W. Cheong, *Phys. Rev. Lett.* **75**, 3336 (1995).
4. P.G. Radaelli, D.E. Cox, M. Marezio, and S.-W. Cheong, *Phys. Rev.* **B55**, 3015 (1997).
5. J.B. Goodenough, *Phys. Rev.* **100**, 564 (1955).
6. E.O. Wollan and W.C. Koehler, *Phys. Rev.* **100**, 545 (1955).
7. A.P. Ramirez, P. Schiffer, S-W. Cheong, C.H. Chen, W. Bao, T.T. Palstra, P.L. Gammel, D.J. Bishop, and B. Zegarski, *Phys. Rev. Lett.* **76**, 3189 (1996).
8. M.R. Ibarra, J.M. De Teresa, J. Blasco, P.A. Algarabel, C. Marquina, J. Garc'a, J. Stankiewicz, and C. Ritter, *Phys. Rev.* **B56**, 8252 (1997).
9. R.K. Zheng, G. Li, A.N. Tang, Y. Yang, W. Wang, X.G. Li, Z.D. Wang, and H.C. Ku, *Appl. Phys. Lett.* **83**, 5250 (2003).
10. M. Pissas and G. Kallias, *Phys. Rev.* **B68**, 134414 (2003).
11. P.G. Radaelli, D.E. Cox, M. Marezio, S-W. Cheong, P.E. Schiffer, and A.P. Ramirez, *Phys. Rev. Lett.* **75**, 4488 (1995).
12. Y. Yoshimara, P.C. Hammel, J.D. Thompson, and S-W. Cheong, *Phys. Rev.* **B60**, 9275 (1999).
13. M. Roy, F.J. Mitchell, A.P. Ramirez, and P.E. Schiffer, *J. Phys.: Condens. Matter* **11**, 4834 (1999); M. Roy, F.J. Mitchell, A.P. Ramirez, and P.E. Schiffer, *Phys. Rev.* **B58**, 5185 (1998).
14. R. Mahendiran, M.R. Ibarra, A. Maignan, C. Martin, B. Raveau, and A. Hernando, *Solid State Commun.* **111**, 525 (1999).
15. F. Damay, C. Martin, A. Maignan, and B. Raveau, *J. Appl. Phys.* **82**, 6181 (1997).
16. P. Levy, F. Parisi, G. Polla, D. Vega, G. Leyva, H. Lanza, R.S. Freitas, and L. Ghiveder, *Phys. Rev.* **B62**, 6437 (2000).
17. G. Adolli, R.De Renzi, F. Licci, and M.W. Pieter, *Phys. Rev. Lett.* **81**, 4736 (1998).
18. J. Dho, I. Kin, and S. Lee, *Phys. Rev.* **60**, 14545 (1999).
19. S. Mori, C.H. Chen, and S-W. Cheong, *Phys. Rev. Lett.* **81**, 3972 (1998).
20. W. Tong, Y. Tang, X. Liu, and Y. Zhang, *Phys. Rev.* **B68**, 134435 (2003).

21. J.C. Loudon, N.D. Mathur, and P.A. Midgley, *Nature* (*London*) **420**, 797 (2002); *J. Magn. Magn. Mater.* **272–276**, 13 (2004).
22. E. Dagotto, T. Hotta, and A. Moreo, *Phys. Rep.* **344**, 1 (2001).
23. A.J. Millis, *Phys. Rev.* **B53**, 8434 (1996).
24. K.H. Ahn and A.J. Millis, *Phys. Rev*. **B58**, 3697 (1998); *ibid*. **61**, 13545 (2000).
25. M.J. Calderón, A.J. Millis, and K.H. Ahn, *Phys. Rev.* **B68**, 100401 (2003).
26. A. Biswas, M. Rajeswari, R.C. Srivastava, Y.H. Li, T. Venkatesan, R.L. Green, and A.J. Millis, *Phys. Rev.* **B61**, 9665 (2000).
27. A. Biswas, M. Rajeswari, R.C. Srivastava, T. Venkatesan, R.L. Green, Q. Lu, A.L. de Lozanne, and A.J. Millis, *Phys. Rev*. **B63**, 184424 (2001).
28. V.G. Prokhorov, V.A. Komashko, V.L. Svetchnikov, Y.P. Lee, and J.S. Park, *Phys. Rev*. **B69**, 014403 (2004).
29. E.B. Nyeanchi, I.P. Krylov, X.-M. Zhu, and N. Jacobs, *Europhys. Lett.* **48**, 228 (1999).
30. V.G. Prokhorov, G.G. Kaminsky, V.A. Komashko, J.S. Park, and Y.P. Lee, *J. Appl. Phys.* **90**, 1055 (2001).
31. K.H. J. Buschow and F.R. de Boer, *Physics of Magnetism and Magnetic Materials*, Kluwer Academic/Plenum, New York (2003).
32. G. Xiao, G.Q. Geong, E.J. McHiff, and A. Gupta, *J. Appl. Phys.* **81**, 5324 (1997).
33. C.H. Chen and S-W. Cheong, *Phys. Rev. Lett.* **76**, 4042 (1996).
34. D. Rubi, S. Duhalde, M.C. Terzzoli, G. Leyva, G. Polla, P. Levy, F. Parisi, and R.R. Urbano, *Physica* **B320**, 86 (2002).
35. M. Malfait, I. Gordon, V.V. Moshchalkov, Y. Bruyneraede, G. Borghs, and P. Wagner, *Phys. Rev.* **B68**, 132410 (2003).
36. Y. Xiong, S.-Q. Shen, and X.C. Xie, *Phys. Rev.* **B63**, 140418 (2001).
37. J. Appel, *Phys. Rev.* **141**, 506 (1966).
38. B.D. Cullity, *Introduction to Magnetic Materials,* Addison-Wesley, New York (1972).
39. S. Bueble, K. Knorr, E. Brecht, and W.W. Schmahl, *Surf. Sci.* **400**, 345 (1998).